ARL-TN-0890 ● June 2018

US Army Research Laboratory

Effect of Porosity on Synthetic Sand Infiltration within Yttria-Stabilized Zirconia Pellets

by Andrew Wright, Michael Walock, Andy Nieto, Anindya Ghoshal, Jian Luo, and Muthuvel Murugan

NOTICES

Disclaimers

The findings in this report are not to be construed as an official Department of the Army position unless so designated by other authorized documents.

Citation of manufacturer's or trade names does not constitute an official endorsement or approval of the use thereof.

Destroy this report when it is no longer needed. Do not return it to the originator.

ARL-TN-0890 ● June 2018

US Army Research Laboratory

Effect of Porosity on Synthetic Sand Infiltration within Yttria-Stabilized Zirconia Pellets

by Andrew Wright and Jian Luo
Department of Nanoengineering, University of California – San Diego

Michael Walock, Andy Nieto, Anindya Ghoshal, and Muthuvel Murugan
Vehicle Technology Directorate, ARL

REPORT DOCUMENTATION PAGE

Form Approved
OMB No. 0704-0188

1. REPORT DATE *(DD-MM-YYYY)*	2. REPORT TYPE	3. DATES COVERED (From - To)
June 2018	Technical Note	1 May–31 August 2017

4. TITLE AND SUBTITLE
Effect of Porosity on Synthetic Sand Infiltration within Yttria-Stabilized Zirconia Pellets

5a. CONTRACT NUMBER

5b. GRANT NUMBER

5c. PROGRAM ELEMENT NUMBER

6. AUTHOR(S)
Andrew Wright, Michael Walock, Andy Nieto, Anindya Ghoshal, Jian Luo, and Muthuvel Murugan

5d. PROJECT NUMBER

5e. TASK NUMBER

5f. WORK UNIT NUMBER

7. PERFORMING ORGANIZATION NAME(S) AND ADDRESS(ES)
US Army Research Laboratory
ATTN: RDRL-VTP
Aberdeen Proving Ground, MD 21005-5066

8. PERFORMING ORGANIZATION REPORT NUMBER
ARL-TN-0890

9. SPONSORING/MONITORING AGENCY NAME(S) AND ADDRESS(ES)

10. SPONSOR/MONITOR'S ACRONYM(S)

11. SPONSOR/MONITOR'S REPORT NUMBER(S)

12. DISTRIBUTION/AVAILABILITY STATEMENT
Approved for public release; distribution is unlimited.

13. SUPPLEMENTARY NOTES
This work is in support of a DOD Laboratory-University Collaborative Initiative.

14. ABSTRACT
Sand infiltration was investigated for several yttria-stabilized zirconia (YSZ) pellets of varying porosity. The pellets were synthesized through either pressureless spark plasma or cold sintering. As-sintered pellets were exposed to molten and semi-molten synthetic sand for approximately 15 min each. Several characterization techniques were used to correlate the sand infiltration to porosity. It was found that there was no significant difference in the results of low and high porosity samples. Interestingly, sand had infiltrated all samples to some degree although the magnitude of the infiltration did not appear to be related to the porosity. Electron micrographs of a low-porosity sample indicate an infiltration mechanism through the YSZ grain boundaries. X-ray diffraction detected the presence of quartz, which is seen to add strain into the system. Lastly, isotropy and surface roughness tests suggest a general increase in both parameters in all samples but no difference was seen between the high and low porosity samples. Possible mechanisms include infiltration through the grain boundaries and a reactive grain boundary-like mechanism due to Y3+ leaching out of the YSZ crystal structure to form a yttrium silicate phase.

15. SUBJECT TERMS
molten sand infiltration, thermal barrier coatings, yttria-stabilized zirconia, YSZ, porosity

16. SECURITY CLASSIFICATION OF:			17. LIMITATION OF ABSTRACT	18. NUMBER OF PAGES	19a. NAME OF RESPONSIBLE PERSON
a. REPORT	b. ABSTRACT	c. THIS PAGE			Michael J Walock
Unclassified	Unclassified	Unclassified	UU	26	19b. TELEPHONE NUMBER (Include area code) 410-278-9018

Standard Form 298 (Rev. 8/98)
Prescribed by ANSI Std. Z39.18

Contents

List of Figures

List of Tables

1. Introduction

Thermal barrier coatings (TBCs) have been applied on turbine vanes and blades to protect the underlying metal from thermal effects as early as 1970.[1,2] Before 1985, turbines typically operated with no cooling efforts since the temperatures faced at the turbine only reached up to 1100 °C. With the introduction of film cooling in 1985 and the subsequent increase in combustion chamber temperature, TBCs were used to protect the nickel superalloy from melting. With this increase in temperature, a new problem of degradative molten sand attack was faced.

TBCs typically consist of a bond coat, a ceramic top coat, and a thermally grown oxide layer sandwiched between the two, which inevitably develops due to oxidation of the bond coat. The ceramic top coat, consisting usually of yttria-stabilized zirconia (YSZ), is the first line of defense and experiences the austere conditions faced from the exhaust of the combustion chamber. The issues wrought by sand-induced degradation are collectively known as CMAS attack, named after the general chemistry exhibited by many environmental particulates including sand (calcia-magnesia-alumina-silicates [CMAS]).

Some turbofan jet engines have dry, mesh filters located behind the fans that break up larger particles to reduce the chance of large particles causing erosion on the coating. Smaller particles are free to pass through the engine unhindered, where they then undergo partial liquidizing through the combustion chamber and contact the TBC on the turbine. Conditions like this are encountered in dust-laden environments such as Southwest Asia, but are also present in regions with volcanic ash or dust in the atmosphere, which has been shown to have similar effects.[3,4] Several mechanisms of failure have been attributed to sand, depending on the temperature of the free stream. Such failures have been known to be caused by cracks, delaminations from the bond and top coats, erosion, deposit formation, and wrinkling.[5] With continual efforts to increase the operating temperatures and engine efficiency, these sand-induced problems have become exacerbated. A significant effort is now in progress to look at the design of TBCs and reduce the effects of sand on such structures, whether it be with new materials or improvements in design. A full characterization of CMAS infiltration mechanisms and chemical reactions is needed, to determine the mechanism of how molten sand infiltration through the top coat can be mitigated or minimized.

In this report, a small portion of the CMAS attack mechanism characterization goal is examined. Precisely, the effect of the porosity (or density) of the top coat material on sand infiltration was investigated. This was accomplished by preparing pellets of YSZ with densities ranging from approximately 40% to 99%. Pretest and posttest

characterization involved density, X-ray diffraction (XRD), scanning electron microscopy (SEM) with energy dispersive spectroscopy (EDS), confocal laser scanning microscopy (C-LSM), and scanning acoustic microscopy (SAM). Sand testing was conducted by means of partial melting of the sand already in contact with the pellets. The pellets were buried in sand within a container. The temperature on the upper surface of the container was controlled to be around 1300 °C by means of a welding torch flame. The use of the welding torch on the top surface, coupled with cooling air on the bottom surface, allowed for a thermal gradient to exist within the container to mimic some of the conditions faced in engines. The evolution of crystal structures and the appearance of new phases, increases in surface roughness and isotropy, and microstructural characteristics along with possible routes of infiltration are detailed in the results.

2. Materials and Methods

2.1 Powder Characterization

Approximately 20 YSZ pellets of varying composition (3 mol% [3YSZ], 4 mol% [4YSZ], and 8 mol% [8YSZ]), sintering methods (conventional, spark plasma, and cold sintering), and dimensions (diameter: 0.25 to 1 inch, thickness: 1 to 6 mm) were tested.

The as-received 4 mol% (~7 wt%) powder (Metco 204NS, Metco Oerlikon, Switzerland) was high-energy ball milled (8000D Mixer/Mill, SPEXSamplePrep, NJ) in isopropyl alcohol using zirconia media with two 0.5-inch zirconia balls for 6 h. The milled powder was then dried at 80 °C overnight and then lightly grinded with an agate mortar and pestle to break up any agglomerates. The powder was compacted in a 1-inch internal diameter (ID) stainless steel die under 60 MPa for approximately 2 min. The 3YSZ (99.95%, 20 nm, US Research Nanomaterials Inc, TX) and 8YSZ (TZ-8Y, 40 nm, Tosoh Corporation, Japan) nanopowders were both used as-received. The 8YSZ powder was pressed under the same conditions as the 4YSZ powder to receive a green pellet.

2.2 Sintering

The green pellets (4YSZ and 8YSZ) were sintered through either the conventional sintering or spark plasma sintering (SPS). A 2-step sintering procedure was used for the conventional method. The pellet was heated from room temperature to 1000 °C in air at 5 °C/min and held for 1 h and then further treated at 1000–1500 °C at 5 °C /min with a dwell time of 2 h before naturally cooling in the furnace. For SPS, the powder was pressed at 50 MPa and heated to 1150–1800 °C in argon at a

rate of 100 °C/min and a dwell time of 2–5 min. The temperature was controlled by a pyrometer. The pellets naturally cooled in the machine with 5 MPa of pressure applied to enhance the cooling rate. The YSZ samples were then decarburized at 1150 °C with a ramp of 5 °C/min for 12 h.

The 3YSZ nanopowder underwent a relatively new technique to form a pellet, called cold sintering. The process is explained in detail in an outside source,[6] so the procedure stated here will be brief. The powder was combined with 20 wt% DI water and mixed with an agate mortar and pestle for 90 s to achieve a homogenous mixture. The resulting slurry was transferred into a 0.25-inch ID stainless steel die. The slurry was isostatically pressed at 350 MPa and immediately heated to 180 °C at a rate of 10 °C/min with a dwell time of 30 min. The pellets naturally cooled in the die and were then dehydrated in a furnace at 200 °C overnight to remove any residual water.

2.3 CMAS Attack Flame Test

The experimental setup used to induce sand infiltration within the YSZ pellets is shown in Fig. 1, named button cell flame test rig (BCFTR).

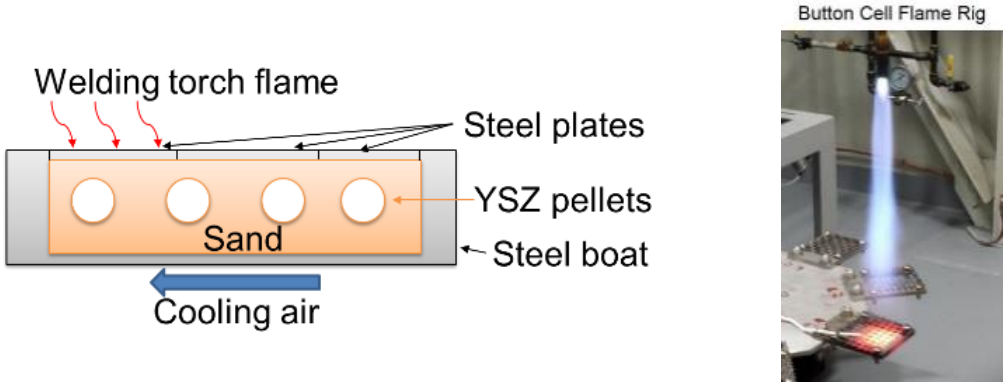

Fig. 1 a) Schematic of BCFTR experimental setup; b) photo of welding torch in relation to holder

A steel boat was prepared by packing it with synthetic sand (AFRL-02, Powder Technology Incorporated, MN) and burying a few YSZ pellets within the sand. Three thin metal plates were placed across the top of the boat to prevent sand from spraying out due to the velocity of the torch. The welding torch was positioned approximately 2 ft above the steel boat. Once the welding torch was ignited, the flame was adjusted so that the flame was concentrated on 1 of the 3 metal plates. Each metal plate was exposed to the flame for 15 min for a total runtime of 45 min. The height of the welding torch in relation to the boat was also adjusted to control the temperature. The temperature was controlled by checking a dual wavelength

pyrometer measuring the surface temperature of the tested steel plate. The height of the torch was adjusted manually and pyrometer temperature was inspected visually so that it was approximately 1300 °C—no automatic controller was set. Compressed air was blown on the underside of the boat by an air knife to provide backside cooling as seen in turbines.

2.4 Characterization Techniques

2.4.1 Density

The relative density of the pellets was calculated by either mass/geometry or Archimedes method according to ASTM C373-16e1,[7] which involves placing the pellets in boiling water for 5 h to remove any gas in the pores. The theoretical density was taken to be 5.95 g/cm^3 (8YSZ) or 6.08 g/cm^3 (3YSZ and 4YSZ).

2.4.2 Confocal Laser Scanning Microscopy (C-LSM)

A C-LSM (Leica Microsystems, IL) was used at 50× magnification and primarily used the Z-stacking function. This procedure used a 462-nm laser and took several images with 1 μm step size in the z-axis to reconstruct a topographical map of the sample site (~300 × 300 μm). Data files from the images were exported to an external program where the surface roughness and isotropy values were calculated. Three to 5 data points were collected for each sample.

2.4.3 Scanning Acoustic Microscopy (SAM)

An overall topographical map was obtained by an SAM (Gen6, Sonoscan, Inc, IL). The SAM used a 100-MHz transducer positioned approximately 2 cm above the sample in water at 40 °C. The instrument was operated in reflection mode. As the acoustic wave was raster-scanned across the sample, a surface map was revealed that could detail relatively flat areas within the sample. Locations featuring significant surface roughness or voids within the sample would be attributed as no signal in the resulting map due to scattering of the waves or high attenuation of acoustic waves in air, respectively.

2.4.4 X-Ray Diffraction (XRD)

XRD was carried out using a Bruker D2 Phaser benchtop XRD with a Cu-kα (0.15418 nm) source. The diffraction was scanned from 20° – 80° 2θ with a 0.05° step and a dwell time of 3 s per step. Prior to measurement, the samples were polished down to at least 1200 grit using SiC sandpaper. The resulting diffraction pattern was Rietveld analyzed using the TOPAS software. The refinement was used to get insight on the lattice parameters, strain within the crystal structure, and estimate of the tetragonal-to-cubic phase ratio. In achieving this, the Lorentzian

crystallite size and strain could vary for both tabulated tetragonal and cubic patterns.

2.4.5 Scanning Electron Microscopy (SEM)

The microstructure effects of the CMAS infiltration were examined by an SEM (Hitachi S4700, Germany) equipped with an EDS and back-scatter electron detector. The accelerating voltage and working distance used 5.0 kV and 5 mm, respectively. All samples were coated using a sputter coater (Desk V, Denton Vacuum, NJ) with an Au-Pd target prior to examination. Cross sections were polished down to 0.5 μm by use of diamond lapping films and then sputtered. All specimens were attached to the SEM mount by double-sided carbon tape. Copper tape was also attached to the sample and stage in an extra effort to negate charging.

3. Results/Discussion

3.1 Density

The synthetic sand was previously known to melt around 1100 °C.[8] A 15-min exposure time at 1300 °C was shown to provide ample CMAS interaction with the pellets. This was seen visually through the pretest and posttest photos in Fig. 2.

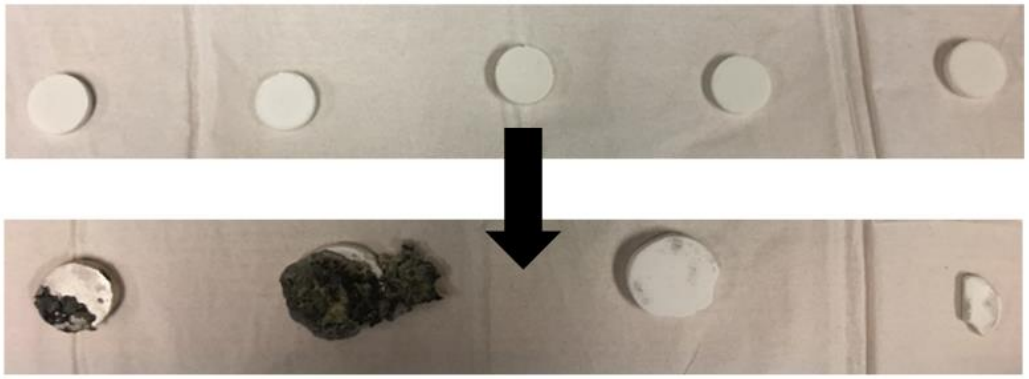

Fig. 2 a) Pretest and b) posttest images following sand testing. Large deposits are clearly seen in some of the samples while others only show signs of infiltration through color changes.

Preceding testing, all pellets were white, with thicknesses varying from 1–6 mm, and diameters varying from 6–25 mm. Following testing, changes in the form of glassy, siliceous deposits or gray infiltration regions are seen in all samples, regardless of density. No preference for deposit formation based on density was noticed, however.

Posttest density measurements determined through Archimedes method for porous specimens were followed to gain insight on the mass and volume of sand infiltrated.

This can only be applied assuming there are no deposits on the surface. The samples with significant deposit formation were treated no differently than the pellets without deposits. This was done to not disturb the microstructure at the CMAS-YSZ interface. Disruption may involve CMAS withdrawing from the YSZ and leaving empty pores. The comparison between the densities preceding and following testing is shown in Fig. 3.

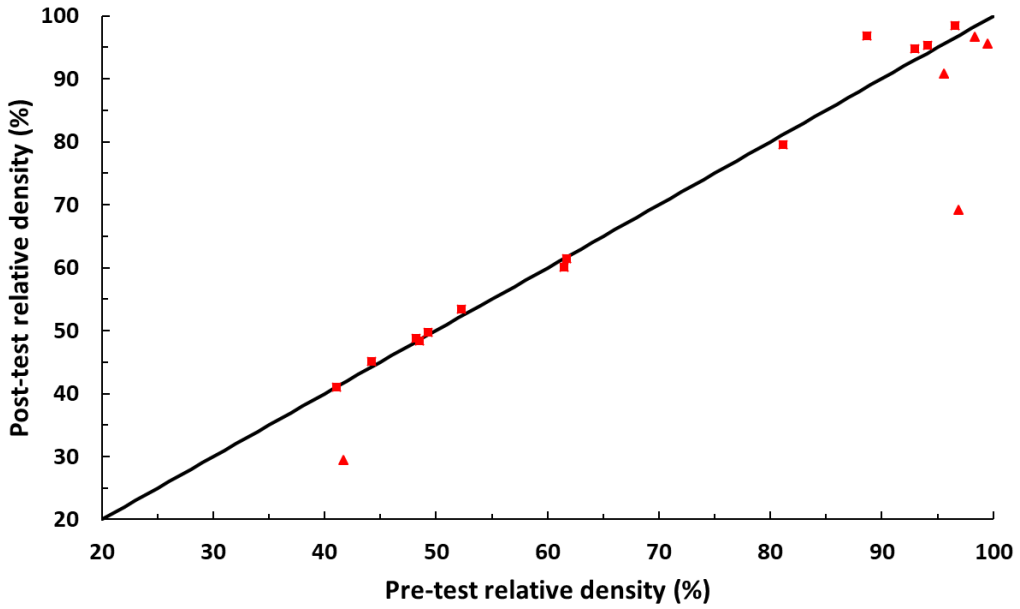

Fig. 3 Comparison between pretest and posttest densities. Black, x = y line represents no change in density following testing. Data points denoted with red triangles signify samples with significant CMAS deposition.

Nearly all points fall within the error of ±2% of the x = y line. Significant decreases in density are due to samples bearing large, porous surface deposits that are primarily composed of silica, which is less dense than YSZ. No substantial differences are seen between the low- and high-density samples.

Accumulation rates are calculated by dividing the total mass of sand accumulated by the exposure time (15 min). They appear to be approximately 10–20 μg/s based on the data in Table 1. Nearly half the samples show loss of mass following testing. This could be attributed to the strong CMAS adhesion along with the weak YSZ internal strength due to the high porosity causing significant strain leading to slow erosion of the pellets since mass loss tends to occur in low-density samples. In fact, the 47.3% dense pellet was fractured into 2 halves during testing, which may be due to excessive strain within the sample.

Table 1 Data for each pellet revealing the change in mass following CMAS exposure. Asterisk denotes samples barring sand deposits.

Relative Density (%)	Pre-mass (g)	Post-mass (g)	Total mass of sand accumulated (g)	Percent sand added (%)	Accumulation rate (μg/s)
Conventional					
41.1	5.783	4.7728	-1.0102	-17.468	-1122
41.7*	5.581	6.6102	1.0292	18.441	1144
49.3	6.6493	3.675 3.0678	0.0935	1.4062	103.9
61.5*	13.718	12.6608	-1.0572	-7.7067	-1175
61.7	9.554	8.7455	-0.8085	-8.4624	-898.3
81.2	6.567	6.3052	-0.2618	-3.9866	-290.9
88.7	6.458	6.4334	-0.0246	-0.3809	-27.33
95.6*	6.7693	6.9003	0.131	1.9352	145.6
96.6	4.596	4.5974	0.0014	0.0305	1.556
SPS					
93	4.6517	4.6734	0.0217	0.4665	24.11
94.1	6.8683	6.8785	0.0102	0.1485	11.33
96.9*	4.9968	5.6664	0.6696	13.401	744.0
98.4*	8.964	9.0658	0.1018	1.1357	113.1
99.5*	2.0248	2.0264	0.0016	0.0790	1.778
Cold Sintering					
44.2	0.167	0.1439	-0.0231	-13.832	-25.67
48.2	0.147	0.1298	-0.0172	-11.701	-19.11
48.5	0.114	0.0996	-0.0144	-12.632	-16.00
52.3	0.122	0.1097	-0.0123	-10.082	-13.67

3.2 Confocal Laser Scanning Microscopy (C-LSM)

The surface roughness and degree of isotropy was examined for each of the pellets before and after testing using a C-LSM. Topographical maps of area 300 μm × 300 μm were reconstructed using Z-scan imaging. Examples of the surface maps are shown in Fig. 4.

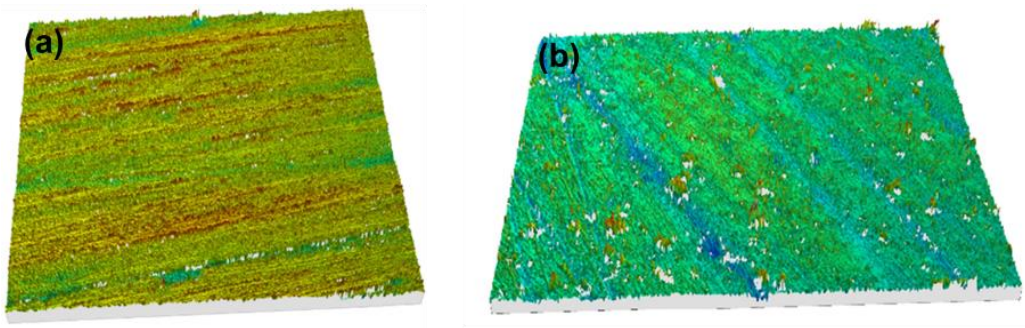

Fig. 4 a) Pretest and b) posttest surface maps of a high-density (93.0%) pellet. Small peaks in the post image are suggested to be randomly distributed sand deposits.

Surface roughness values were calculated in accordance to the ISO 25178.[9] In this example, the surface roughness was seen to increase from 0.548 to 0.593. This can be identified through the numerous plateaus seen in the posttest image arising from small silica deposits on the surface. The degree of isotropy was also measured for each of the samples and using this example the value increased from 10.212% to

17.353% following testing. An increase in surface roughness and isotropy was a general trend that was seen in nearly all samples, regardless of density, as shown in Fig. 5.

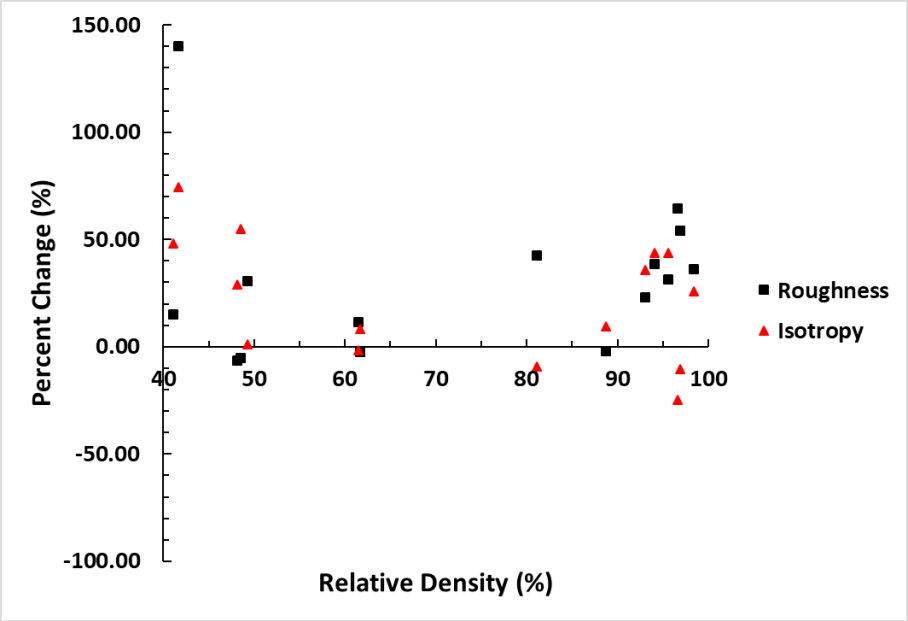

Fig. 5 Percent change in surface roughness and isotropy as a function of relative density. An increase in both variables is discerned.

An increase in both variables could be attributed to a scenario where sand deposits are forming on the surface at random with no preference to previous deposit locations or areas of greater activity. A random distribution of deposits would increase surface roughness by introducing greater height differences within the sample and the isotropy would increase due to the random distribution of the deposits. While there was a general increase in both variables across all densities, Fig. 5 seems to suggest that low-density samples experience higher degrees of isotropy increase while high-density samples experience higher surface roughness gains. A possible explanation is that in high-density samples the sand deposits form near each other on flat surfaces, away from valleys, while in low-density samples the sand deposits form within the valleys (not near each other).

3.3 Scanning Acoustic Microscopy (SAM)

While C-LSM was used to determine surface roughness and isotropy on a micron-sized scale, the SAM was used to get a detailed macroscopic view of the surface. The SAM featured a 100-MHz transducer that was raster scanned across the sample to provide a surface map. Figure 6 shows a case of a high-density (93.0%) sample.

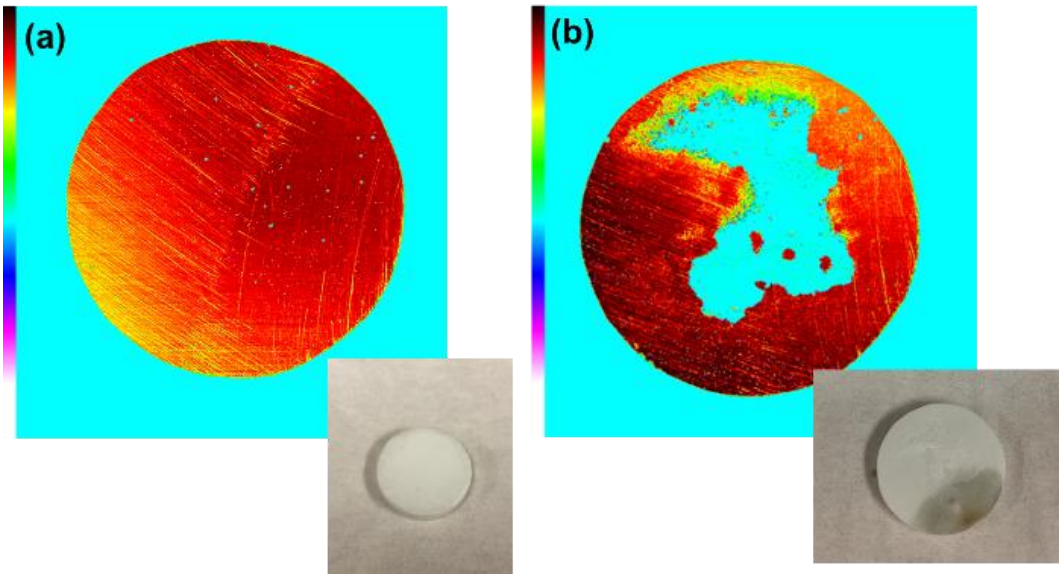

Fig. 6 a) Pretest and b) posttest SAM surface maps along with optical images of a 93.0% dense pellet. A white sand deposit is seen spanning across the surface while heavy sand infiltration (seen as discoloration) is discerned in the posttest sample. The color map corresponds to elevation (small time of flight) in the sample with red/black, purple, and light blue representing high elevation, low elevation, and no signal, respectively. No signal rises from either scattering (from rough sand deposits) or bubbles on the surface (high attenuation in air).

Grinding patterns are easily distinguishable in the pretest image along with small blue dots, which are due to bubbles forming on the surface during the scan. Following testing, a large white sand deposit was seen, optically and through the SAM, across the surface. The deposit appears as no signal because, due to the height, the deposit was out of focus and the acoustic waves are scattered away from the detector located in the transducer. Grinding patterns are still discerned; however, the gradient is flipped and appears of greater magnitude within the YSZ surface. This may be due to deposits on the backside or because the surfaces of the pellets were not flat. The discolored region denoting infiltration does not seem to have a noticeable effect on the surface topography of the sample. Grinding lines are still, with near same resolution, visible as in the pretest image suggesting very little (i.e., thin) deposit formation occurred and sand primarily diffused through this sample. This technique was performed for all samples; however, no differences were seen between the high- and low-density samples that the C-LSM did not already identify.

3.4 X-Ray Diffraction (XRD)

XRD was also carried out before and after testing. A large majority of the samples are seen to be YSZ with no contaminants (a few appear to have vanadium and iron

contamination). For each XRD pattern, Rietveld refinement was carried out to get an idea on the ratio of tetragonal to cubic phase of YSZ within the samples. The Lorentzian crystallite size and strain were also refined for each tabulated pattern. This was done to gain insight on peak broadening and shifts that may occur. Figure 7 shows the pretest and posttest XRD patterns for a low- and high-density sample.

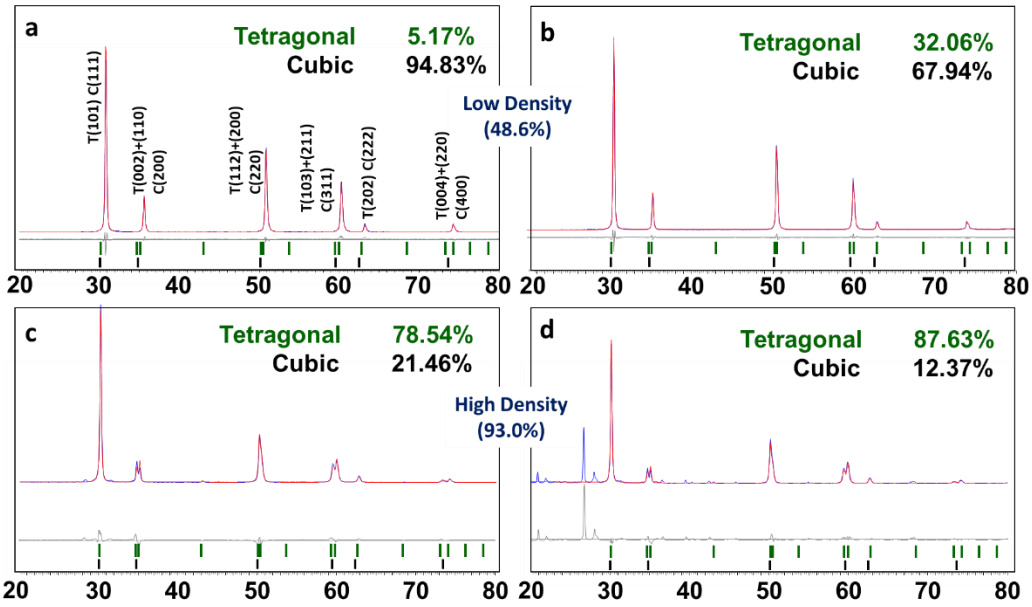

Fig. 7 Rietveld-analyzed XRD patterns for a (a, b) low- and (c, d) high-density sample with (a, c) pretest and (b, d) posttest patterns to see the effects of CMAS testing. Blue, red, and gray patterns represent experimental, Rietveld fitting, and the difference between the two, respectively. The green and black dashes below the curves are the simulated peak positions for the tetragonal and cubic phase. The composition of the low- and high-density sample are 8YSZ and 4YSZ, respectively.

Three features to note are the addition of new phases, peak shift, and the change in tetragonal to cubic phase ratio. A few new peaks are seen in the high-density sample around 21, 27, and 29° 2θ. These new peaks are suggested to be attributed to quartz and cristobalite. Negative peak shifts were examined for both samples but the magnitude of the shift is different. The 48.6% dense sample experienced a 0.2° 2θ shift while the 93.0% dense sample negatively shifted 0.05° 2θ. A majority of the samples underwent a negative shift following testing with only a couple of them shifting positively. Positive and negative peak shifts are usually suggested to be due to compressive and tensile strain,[10] respectively. Lastly, an increase in the tetragonal phase content was seen for both pellets. It might be expected that the cubic content would rise for the low-density sample (8YSZ) due to the tetragonal to cubic phase transition around 1150 °C. However, in the low-density sample the infiltrated silica may provide preference for the tetragonal phase to form by

introducing strain into the system coupled with the slow cooling rate and short exposure time.

Further analysis of the Rietveld-refined data was focused on the strain within the samples. Figure 8 shows the change in strain in the tetragonal and cubic phase of each sample following testing. Although the low-density samples seem to have very little changes in strain, the high-density samples appear to have a large decrease in their strain following testing. This could be due to leaching of Y^{3+} out of the YSZ crystal structure and reacting with Si to form a yttrium silicate phase. This phenomenon has been examined and studied in the solid oxide fuel cell field[11] as yttrium loss leads to significant decreases in ionic conductivity. Continual removal of yttrium ions from YSZ will lead to phase changes as pure zirconia will form at the surface of the grains in contact with the CMAS intergranular film at the grain boundary. The strain produced here may be significant but it is hard to conclude with only XRD data. Dedicated strain experiments need to be made using a strain gauge or a similar instrument to arrive at a more definitive claim.

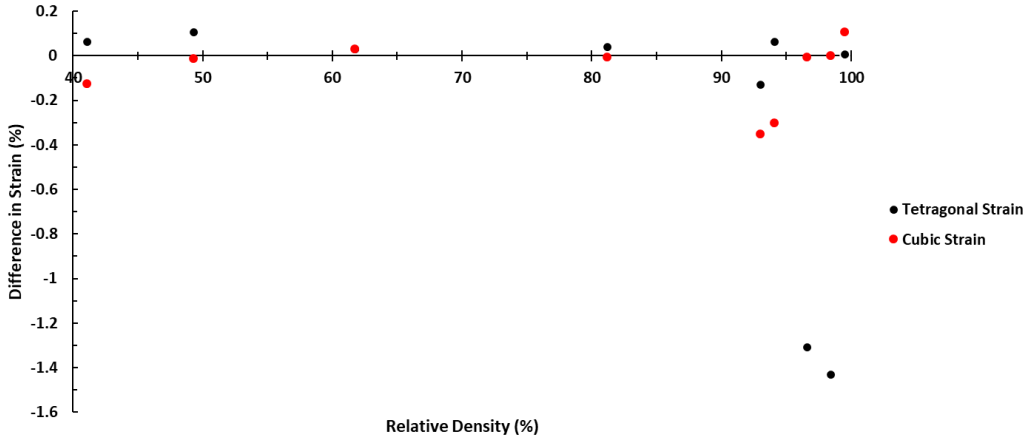

Fig. 8 Change in strain for both the tetragonal and cubic phase for all pellets. Data was collected through the Rietveld-analyzed XRD patterns.

3.5 Scanning Electron Microscopy (SEM)

SEM was used to investigate the microstructure of YSZ pellets exposed to molten sand during the flame test. Figure 9 details a few of the images taken on the top surface of the pellet before and after testing of a high-density (93.5%) sample.

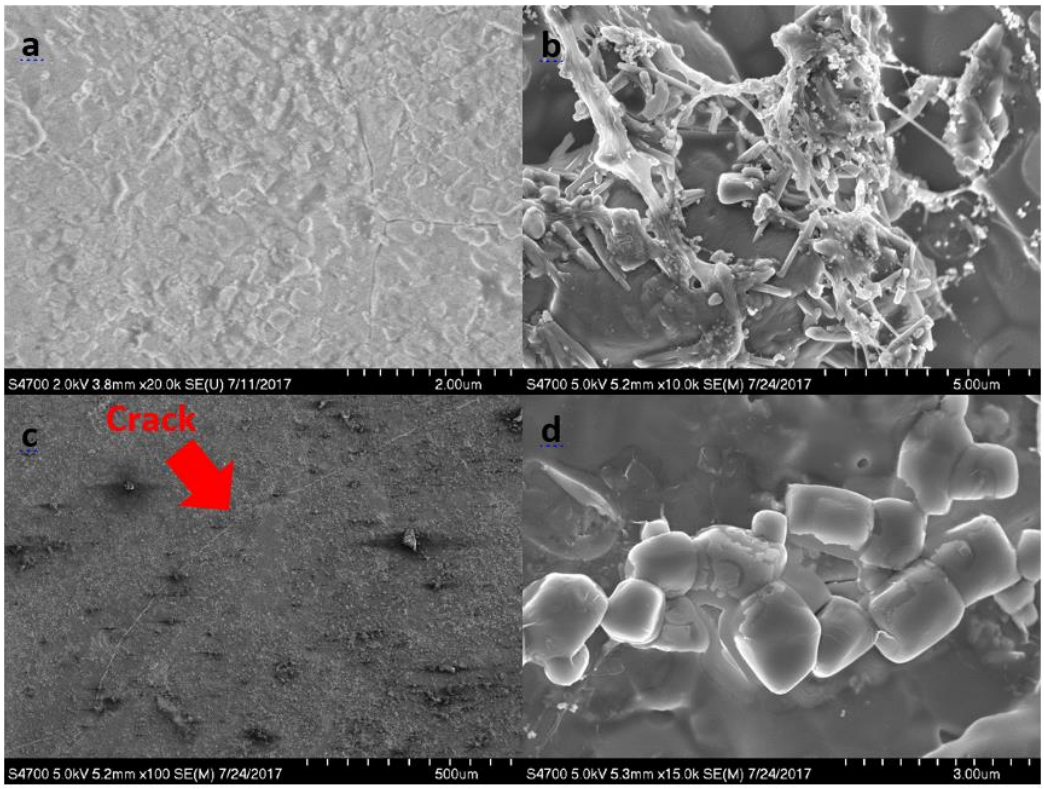

Fig. 9 a) Surface micrograph of a 93.5% density pellet preceding testing. Posttest SEM surface images of the same pellet at different magnification: b) closeup of the sand deposit shows fiber-like strands, which may indicate partial melting; c) a crack of about 30 nm spans across the surface and is discerned as a white line (highlighted by a red arrow); d) at increased magnification, particles are shown to agglomerate along the site of the crack. These particulates are likely to be YSZ grains that have become dislodged from the pellet during thermal cycling since they are consistent in size and morphology of the preexisting grains.

In the initial image (Fig. 9a) the surface is clean, a grain size of about 1 μm can be discerned, and a microcrack is visible on the right side of the image, which most likely formed during processing. Following sand testing, deposits can be seen on the surface in Figs. 9b and c. Particularly in Fig. 9b, fiber-like strands are seen within a deposit adhered to the YSZ surface. This suggests that the sand is undergoing partial melting and, upon cooling, creating these thin fibers. Several of the deposits, which are littered across the surface, exhibit these same characteristics. The knowledge of partial liquefying can help tremendously on pinpointing exact mechanisms of infiltration through further testing. A crack is also discerned on the surface as a white line, and upon increased magnification the white lines appear as structures near or covering the crack as seen in Fig. 8d. These structures are likely to be YSZ grains that have become dislodged during the flame test (thermal cycling). The YSZ grains (~1 μm), which can be seen in the background of Fig. 9b, do not have the same morphology as the sand deposits, which have more irregular shapes, fiber-like strands, and smaller particles adhered

to them. These structures are also seen throughout the entire length of the crack and appear nowhere else on the surface, suggesting that it was a localized phenomenon. These features were also not found in any other sample.

Sand infiltration was also seen penetrating through cracks of a highly dense (99.5%) sample as seen in Fig. 10a. The dark contrasts seen throughout the photo are siliceous compounds penetrating through cracks of the sample, which may be at the site of grain boundaries. This is not suggested to be every grain boundary, as the sizes of these "grains" are too large (~10–20 μm) to be consistent with previous grain sizes on the order of 1 μm. Elemental analysis of the penetration was obtained through EDS, shown in Fig. 10b. The infiltration is clearly shown to be attributed to Si and Ca while the surrounding material is YSZ. Al seems to have partially infiltrated while Mg and Na show very little signs of infiltration. This clearly shows one mechanism of infiltration. If cracks are already present within the sample, which could be formed through thermal expansion, then sand can potentially enter through these sites and fill in the gap. For interactions occurring on the atomic scale, a transmission electron microscopy analysis is needed. It is unknown whether these cracks were present before or after testing. These images are also directly below a sand deposit that formed on the surface, which could have also formed these cracks during testing.

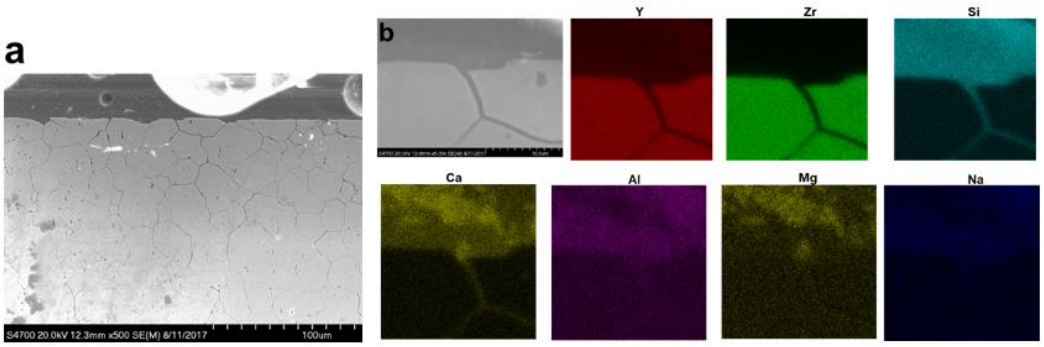

Fig. 10 a) SEM image of a highly dense (99.5%) YSZ sample exhibiting infiltration. The dark contrast at the top of the image is a sand deposit. b) EDS analysis of the infiltration showing Si and Ca to be the main infiltrators.

Another potential mechanism of infiltration (mentioned earlier) involves leaching of Y or Zr out of the crystal structure to form a new compound with Si. Figure 11 shows a few back-scattered SEM images showing great contrast between the bulk YSZ and a suggested Zr-rich phase, due to the lighter contrast. The darker region on top of the lighter region is suggested to be CMAS or Si-rich phases while the bulk is the 4YSZ. This sample has significant porosity (61.5% dense) giving the added capability of the CMAS to infiltrate and particles or atoms to shift around. No elemental analysis has been conducted on this sample yet so these statements

are still speculations. However, if proved correctly, leeching could provide another mechanism of failure by perhaps the weakened structural support of the new Zr-rich phase. SEM analysis provided significant insight on potential mechanisms of infiltration and destruction. However, the results observed were consistent on nearly all samples; no disparities were seen between high- and low-density specimens. Deposits and infiltration sites were present on the majority of samples (as was shown earlier) and on the microscale, the structures and morphology appear to be independent of density.

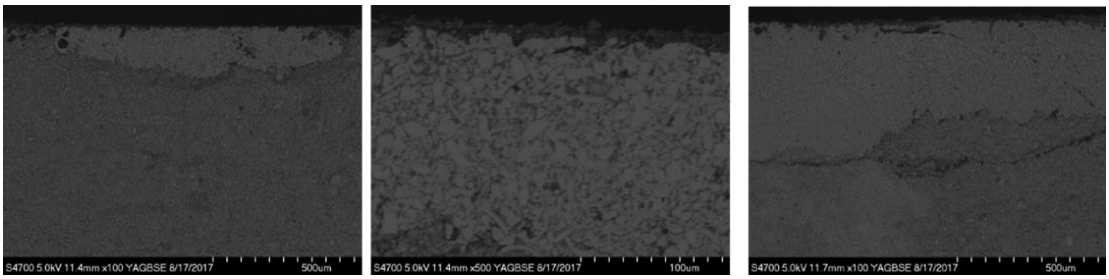

Fig. 11 Back-scattered SEM images of a low-density (61.5%) sample showing 3 different contrast regions: a) 100× magnification of a 3-contrast region; b) increased magnification (500×) of a spot in 11a; c) another, larger 3-contrast region approximately 2 mm to the right of 11a. They are suggested to be dark: Si-rich, light: Zr-rich, and medium: bulk YSZ.

4. Conclusion

In this note, the effect of YSZ porosity was looked at when the material was subjected to sand near its melting temperature (~1100 °C). Sparse differences were noticed through the 5 different characterization techniques used. Density, SAM, and SEM results did not show any significant shifts in data between high- and low-density samples pertaining to CMAS infiltration. Rietveld-analyzed XRD data shows a few new peaks (quartz and a calcium aluminum silicate phase) and also seems to indicate differences in strain within the crystal structure through the effect of peak shifts. C-LSM results show overall increases in surface roughness and isotropy across all samples but may suggest higher increases in isotropy for low-density samples and higher increases in surface roughness for high-density samples. This would indicate different mechanisms of adhering and infiltration depending on density. SEM images show that sand infiltration may be occurring through cracks present in the structure or by a more complicated mechanism of Y^{3+} leaching leading to a reactive grain boundary mechanism. Absence of yttrium within YSZ would form a tetragonal or monoclinic zirconia structure, which is likely to add strain into the system. Overall, density does not seem to be a significant parameter in sand infiltration through YSZ; however, this is still useful as it may be applied to other material systems. The presence of porosity may provide ease of CMAS infiltration, while the absence of porosity may act as an

initial barrier to the infiltration. However, the end result for both cases appears to arrive at a destructive nature, which seems to be history-independent. In other words, a high-density sample may initially slow the kinetics of the CMAS infiltration but after a critical time (likely to be under the 15 min exposure used here), effects are identical to a low-density sample. Time-dependent kinetic/diffusion studies will provide more insight into this hypothesis.

5. References

1. Lynch CT, Mazdiyasni KS, Smith JS, inventors. US Air Force, assignee. Transparent zirconia composition and process for making same. United States patent US 3,432,314. 1969 Mar 11.

2. Boone DH, Goward GW, inventors. United Technologies Corp, assignee. Overhaul process for aluminide coated gas turbine engine components. United States patent US 3,544,348. 1970 Dec 1.

3. Dunn MG, Baran AJ, Miatech J. Operation of gas turbine engines in volcanic ash clouds. J Eng Gas Turbines and Power. 1996;118:724–731.

4. Clarke D, Oechsner M, Padture N. Thermal-barrier coatings for more efficient gas-turbine engines. MRS Bull. 2012;37(10):891–898. doi:10.1557/mrs.2012.232.

5. Levi C, Hutchinson J, Vidal-Sétif M, Johnson C. Environmental degradation of thermal-barrier coatings by molten deposits. MRS Bull. 2012;37(10):932–941. doi:10.1557/mrs.2012.230.

6. Guo H, Guo J, Baker A, Randall CA. Cold sintering process for ZrO2-based ceramics: significantly enhanced densification evolution in yttria-doped ZrO2. J Am Ceram Soc. 2017;100:491–495.

7. Ghoshal A, Murugan M, Walock MJ, Nieto A, Barnett BD, Pepi MS, Swab J, Zhu D, Kerner KA, Rowe C,Shiao C-Y, Hopkins D, Gazonas G. Molten particulate impact on tailored thermal barrier coatings for gas turbine engine. J Eng Gas Turbines Power 2018; 140: 022601.

8. ASTM C373-16e1. Standard test methods for determination of water absorption and associated properties by vacuum method for pressed ceramic tiles and glass tiles and boil method for extruded ceramic tiles and non-tile fired ceramic whiteware products. West Conshohocken (PA): ASTM International; 2016. www.astm.org.

9. Specification, Geometric Product. Surface texture: areal–part 2: terms, definitions and surface texture parameters. International Standard ISO 2012: 25178-2.

10. Khorsand ZA, Abd Majid WH, Abrishami ME, Yousefi R. X-ray analysis of ZnO nanoparticles by Williamson–Hall and size–strain plot methods. Solid State Sci. 2011;13(1):251–256.

11. Lankin M, Yanhai D, Finnerty C. A review of the implications of silica in solid oxide fuel cells. J Fuel Cell Sci Technol. 2011;8(5):054001.

List of Symbols, Abbreviations, and Acronyms

BCFTR	button cell flame test rig
C-LSM	confocal laser scanning microscopy
CMAS	calcia-magnesia-alumina-silicates
DI	deionized
EDS	energy dispersive spectroscopy
ID	internal diameter
SAM	scanning acoustic microscopy
SEM	scanning electron microscopy
SPS	spark plasma sintering
TBC	thermal barrier coating
XRD	X-ray diffraction
YSZ	yttria-stabilized zirconia

1 (PDF) DEFENSE TECHNICAL INFORMATION CTR DTIC OCA

2 (PDF) DIR ARL
IMAL HRA
RECORDS MGMT
RDRL DCL
TECH LIB

1 (PDF) GOVT PRINTG OFC
A MALHOTRA

1 (PDF) DIR
OUSD-R&E
J LU

2 (PDF) NAVAIR-4.3.4.1
C FAUCETT
C MYERS

1 (PDF) NAVAIR-4.4.4
C ROWE

1 (PDF) NASA GRC LME0
D ZHU

3 (PDF) AFRL-RXCCP
D BALLARD
A KATZ
C PRZYBYLA

1 (PDF) AFRL-RQ
R SIKORSKI

2 (PDF) AMRDEC ADA FP
K KERNER
S KINNEY

1 (PDF) AMRDEC AEP
G KELLOGG

1 (PDF) AMRDEC AEP E
R ARMSTRONG

5 (PDF) ARL
RDRL VTP
W ACOSTA
RDRL WMM D
C MOCK
M PEPI
RDRL WMM E
J SWAB
RDRL WMM F
R DOWDING